Solenoidal optical forces from a plasmonic Archimedean spiral

Mohammad Asif Zaman,* Punnag Padhy, and Lambertus Hesselink
Department of Electrical Engineering, Stanford University, Stanford, California 94305, USA

(Received 1 May 2019; published 31 July 2019)

The optical forces generated by a right-handed plasmonic Archimedean spiral (PAS) have been mapped and analyzed. By changing the handedness of the circularly polarized excitation, the structure can switch from a trapping force profile to a rotating force profile. The Helmholtz-Hodge decomposition method has been used to separate the solenoidal component and the conservative component of the force and quantify their relative magnitude. It is shown that the for right-hand circularly polarized excitation, the PAS creates a significant amount of solenoidal forces. Using the decomposed force components, an intuitive explanation of the motion of micro- and nanoparticles in the force field is presented. Vector field topology is used to visualize the force components. The analysis is found to be consistent with numerical and experimental results. Due to the intuitive nature of the analysis, it can be used in the initial design process of complex laboratory-on-a-chip systems where a rigorous analysis is computationally expensive.

DOI: 10.1103/PhysRevA.100.013857

I. INTRODUCTION

Since their introduction in the 1970s by Ashkin [1,2], optical trapping and manipulation techniques have been used in many fields of science and nanotechnology [3–8]. Conventional single-beam optical tweezers can trap and manipulate particles that are larger than the wavelength of the light source. However, for subwavelength-sized nanoparticles, optical tweezers fail to exert sufficient gradient force for trapping due to the diffraction-limited spot size. To overcome this limitation, near-field plasmonic traps have been developed [9–12]. Plasmonic structures utilize surface plasmon polaritons (SPPs) to create strong localized field-intensity enhancement in a spot size smaller than the diffraction limit. The potential wells created by such a structure are much narrower than that of optical tweezers [9]. In addition, the planar geometry of plasmonic structures allows multiple traps to be fabricated on the same chip for implementing laboratory-on-a-chip (LOC) systems [13–17]. Understanding and modeling the optical forces in the vicinity of a plasmonic trap are necessary to design such systems. For this reason, works related to the optical forces of near-field traps have received significant attention in the literature.

One of the challenges in designing complex optical manipulation platforms is the large computational cost associated with the modeling step. Numerical simulation of a three-dimensional (3D) system with more than three or four optical traps becomes impractical due to the extremely lengthy run time. Modeling and analysis techniques that provide intuitive understanding along with numerical data can be very useful. By understanding the optical forces from a single structure, it can be possible to predict how forces from multiple such structures will interact. Thus, a complex system can be designed without requiring a computationally expensive simulation of the whole device. In this work, we focus on understanding the optical forces near a plasmonic Archimedean spiral (PAS) and present some mathematical techniques that can be used for that purpose.

Spiral plasmonic structures have been successfully used as an on-chip polarimeter [18,19], optical antenna [20], vortex lens [21], optical trap [22], etc. Plasmonic spirals have also been used to generate orbital angular momentum (OAM) [23]. The optical responses of the structure are strongly dependent on the polarizations of the incident light [24,25]. It is possible to create two distinct near-field distributions from the same plasmonic spiral by switching from left-hand circularly polarized (LHCP) excitation to right-hand circularly polarized (RHCP) excitation. As the optical forces depend on the gradient of the near-field intensity distribution, the optical force field generated by the spiral can be altered by changing the polarization of the input light. Tsai *et al.* reported an excellent study where they demonstrated selective trapping or rotation of dielectric microparticles using a PAS with LHCP and RHCP excitations [22]. Usually, complex manipulation of micro- and nanoparticles requires multiple closely placed plasmonic structures [13–15,26]. This approach requires a distinct configuration of plasmonic structures for a specific motion. Having the ability to selectively apply different optical forces to induce a variety of motions using a single structure could be very useful. Such an approach would reduce the number of plasmonic structures required to create a specific particle motion in a LOC system. Also, the same structures can be reused for a different set of motion by controlling the polarization of light. Thus, understanding and analyzing the polarization-dependent optical forces near a PAS could be of significant importance in developing complex LOC systems.

The optical forces near a PAS are less well understood than forces near other plasmonic structures such as nanopillars [10,11], C-shaped engravings [13,27], and bow-tie apertures [28]. Although the polarization response and field distribution

*zaman@stanford.edu

around plasmonic spirals have been well studied [21,24,25], the optical forces generated by the structures have not received the same level of attention. The work of Tsai *et al.* [22] is the only published literature on the topic to date. In that work, the authors calculate one-dimensional (1D) force maps (along the x and y directions) and show the generation of trapping force and rotational force for LHCP and RHCP excitations, respectively. However, they did not report the two-dimensional (2D) or 3D force profile. Although the motion of the microparticle was explained from the 1D force profiles, a 2D or 3D force profile can give more insights into the particle dynamics. In this work, we calculate and analyze the optical force field generated by a PAS in three dimensions. To analyze the force lines in detail, the force field is decomposed into a conservative component and a solenoidal component. The Helmholtz-Hodge decomposition (HHD) technique [29,30] is used to accomplish this. We show that the force is almost purely conservative for the LHCP excitation, whereas the force has a strong solenoidal component for the RHCP excitation (considering a right-handed PAS). By decomposing the force field, the trapping force and the rotational force can be easily understood. Vector-field topology [31,32] is used to visualize the force components. An intuitive understanding of the particle motion is achieved by observing the critical points and the associated force lines (integral lines or streamlines) of the decomposed components. In addition, the insight gained from the analysis can be used for designing a platform with multiple plasmonic structures capable of performing complex manipulation of micro- and nanoparticles.

The HHD method used in this paper has been widely used to analyze fluid flow [33] and electromagnetic fields [34,35]. It has only been recently used to analyze near-field optical traps [30]. The HHD method allows a clearer understanding of the optical force field and the motion of particles under its influence. For trapping force fields, the steady-state position probability density of a micro- or nanoparticle can be calculated from the decomposed components [30,36]. Thus, computationally demanding Brownian dynamics simulation can be avoided. The HHD method can be especially useful for analyzing rotational motion as it can isolate the solenoidal component of a vector field. Since a PAS can generate both trapping forces (gradient forces) and rotational forces, the HHD technique is ideal for analyzing its force field. Along with mapping the force profile around a PAS, this work highlights how the HHD method can be used to analyze such forces. To the best of our knowledge, no such work has appeared in the literature yet. The analysis presented in this paper is general and can be applied to other near-field trapping structures as well.

II. GEOMETRY OF THE STRUCTURE

A 3D schematic of a three-turn right-handed PAS is shown in Fig. 1. A gold film is deposited on top of a glass substrate, and the spiral shape is created by etching or milling the film. A dilute aqueous solution of nano- or microparticles is placed on top of the structure. Optical excitation is provided from the bottom through the glass substrate. Note that the handedness of the spiral is defined from the point of view of the input excitation light. The locus of the Archimedean spiral in polar coordinates is given by

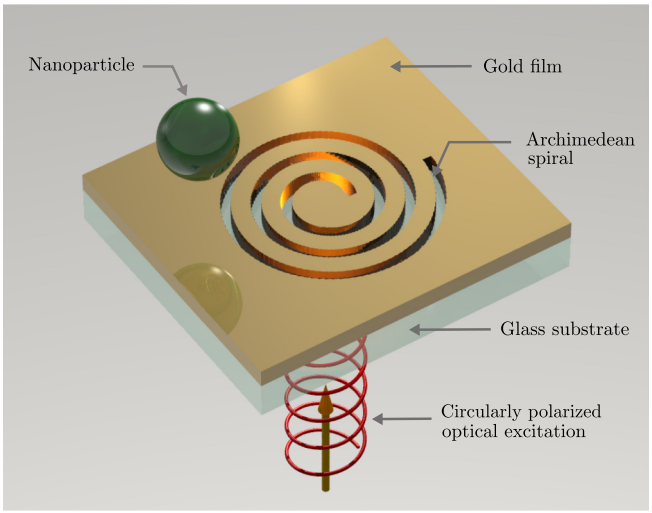

FIG. 1. Schematic of a plasmonic Archimedean spiral.

$$r(\phi) = r_0 + \phi d_{\text{arm}}/2\pi \, . \tag{1}$$

Here r_0 is the initial radius of the spiral, r is the polar radius variable, ϕ is the azimuthal angle variable, and d_{arm} is the radial separation between the arms. ϕ ranges from 0 to 6π for a three-turn spiral. The structure can produce OAM and rotational forces if the SPPs generated from different parts of the spiral interfere in a coherent manner. This occurs when $d_{\text{arm}} = m\lambda_{spp}$, where m is an integer [37]. Here λ_{spp} is the SPP wavelength at the gold-water interface. The current work focuses on the case $d_{\text{arm}} = \lambda_{spp}$ [22,38].

Figure 2 shows the detailed geometry of the structure. The gold film thickness and the air slot width (the width of the spiral arms) are denoted by t_{gold} and d_{air}, respectively. The value of d_{air} should be set sufficiently small so that the radial component of the input illumination can excite and couple SPPs [38]. We consider the excitation wavelength to be 1545 nm. The corresponding SPP wavelength at the gold-water interface is calculated to be 1150 nm. The values of all the geometrical and material parameters relevant for the analysis are listed in Table I [22]. It should be noted that the proper choice of the geometrical dimensions is dependent on the excitation wavelength and material properties. For a different excitation wavelength, the corresponding SPP wavelength at the metal-liquid interface must be determined. From that,

TABLE I. Geometrical and optical parameters.

Parameter	Value
Initial radius of the spiral r_0	2.5 μm
Air slot width d_{air}	300 nm
Thickness of the gold film t_{gold}	250 nm
SPP wavelength at the gold-water interface λ_{spp}	1150 nm
Excitation wavelength λ	1545 nm
Nanoparticle radius r_p	500 nm
Refractive index of water n_w	1.33
Refractive index of polystyrene n_p	1.58

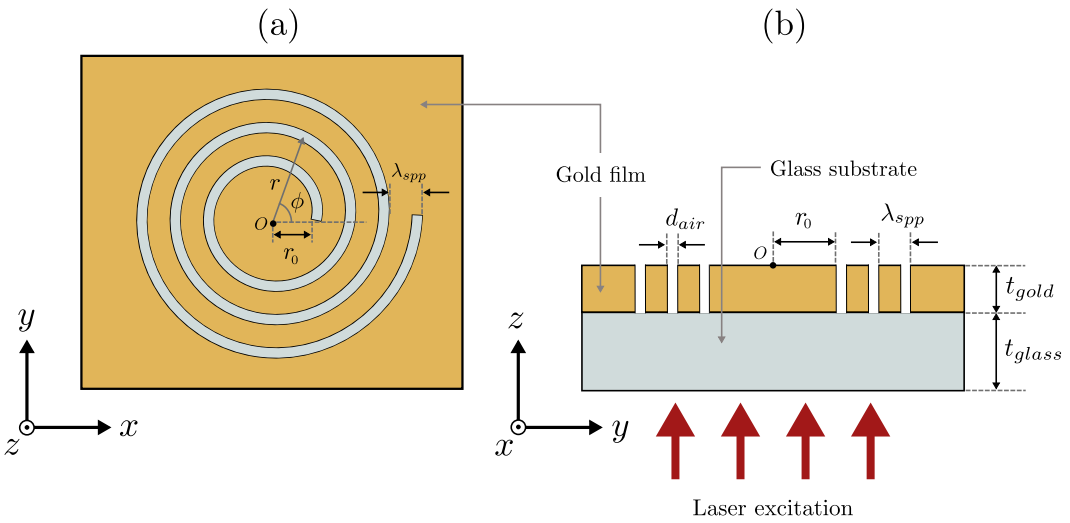

FIG. 2. Geometry of the plasmonic Archimedean spiral. (a) Top view (xy plane). (b) Cross-sectional view (yz plane).

d_{arm} can be calculated. Then the geometry of the structure can be determined using Eq. (1).

III. OPTICAL-FORCE CALCULATION

It is necessary to calculate the electromagnetic-field distribution near the PAS in order to calculate the generated optical forces. For a sufficiently narrow air gap, an approximate analytical equation of the field distribution can be derived for circularly polarized incident light. The expression has the following form [19,39,40]:

$$\mathbf{E}_{spp}(r,\theta,z) \propto \hat{z}\, e^{-k_z z} e^{ik_r r_0} J_q(k_r r). \tag{2}$$

Here $\mathbf{E}_{spp}$ is the electric field generated by the SPPs, $\hat{z}$ is the unit vector along the z direction, (r,θ,z) is the cylindrical coordinate of the observation point, k_z and k_r are the wave numbers in the z and the radial directions, respectively, q is an integer referred to as the *topological charge*, and $J_q(\cdot)$ is the qth-order Bessel function of the first kind. The topological charge is given by $q = s + m$, where s is the spin angular momentum of the incident light and m is related to the geometry of the spiral. For the given geometry ($d_{\text{air}} = \lambda_{spp}$), $m = 1$. The incident light is considered to be circularly polarized (propagating along $+z$), which implies $s = +1$ for RHCP and $s = -1$ for LHCP. So we would expect a field distribution that resembles $J_2(k_r r)$ for RHCP excitation and $J_0(k_r r)$ for LHCP excitation. Although the analytical formulation is approximate and lacks the accuracy for our current analysis, it is helpful in demonstrating that the spiral can create significantly different field distributions depending on the polarization of the input light.

To calculate the field distributions more accurately, we use a commercial finite-element solver (COMSOL MULTIPHYSICS). The optical responses of the structure for LHCP and RHCP excitations are shown in Figs. 3 and 4, respectively. The input field intensity was assumed to be $1 mW/\mu m^2$ for both cases. While localized near-field intensity enhancement can be observed for both cases, the spatial distribution of the near fields is significantly different. In accordance with the analytical formulation, the field distributions shown in Figs. 3(a) and 4(a) resemble the shape of $J_0(k_r r)$ and $J_2(k_r r)$, respectively. It should be noted that the choice of selecting the $z = 10$ nm plane for Figs. 3(a) and 4(a) was arbitrary. However, a plane close to the gold surface ($z = 0$) is preferred for visualization as the strong intensity enhancements occur there.

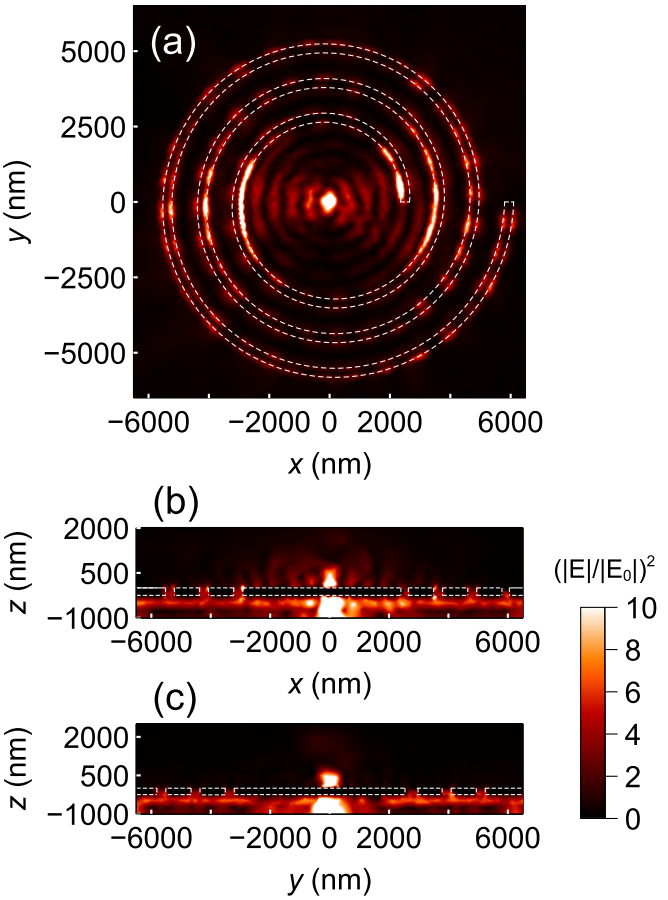

FIG. 3. Field-intensity enhancement for LHCP incident light. (a) $z = 10$ nm plane view, (b) $y = 0$ plane view, and (c) $x = 0$ plane view.

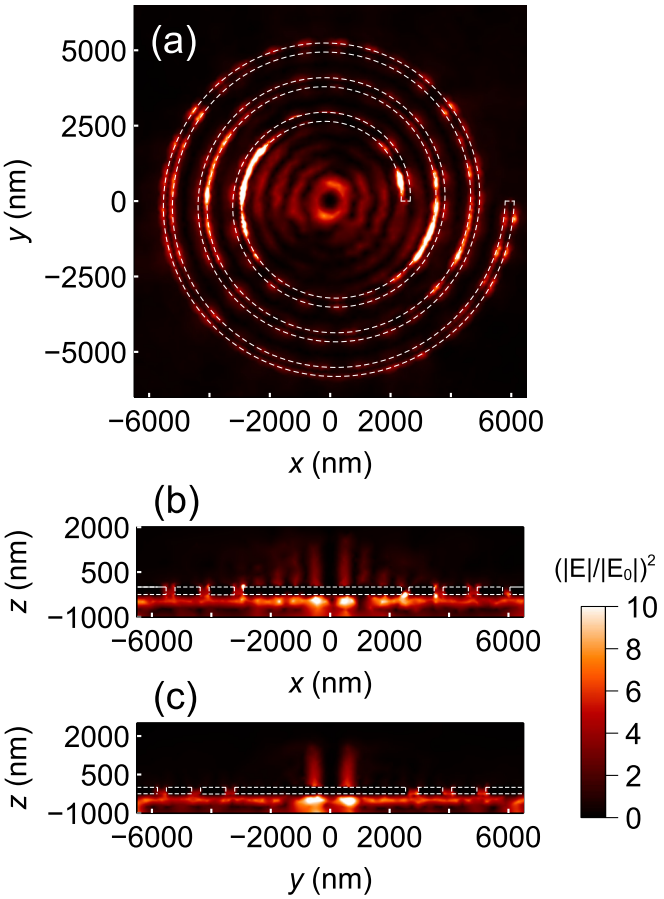

FIG. 4. Field-intensity enhancement for RHCP incident light. (a) $z = 10$ nm plane view, (b) $y = 0$ plane view, and (c) $x = 0$ plane view.

The optical force can be calculated from the electromagnetic-field distribution using the Maxwell stress-tensor formulation:

$$\overleftrightarrow{\mathbf{T}} = \epsilon_w\left(\mathbf{EE} - \frac{1}{2}|\mathbf{E}|^2\overleftrightarrow{\mathbf{I}}\right) + \mu_w\left(\mathbf{HH} - \frac{1}{2}|\mathbf{H}|^2\overleftrightarrow{\mathbf{I}}\right), \quad (3)$$

$$\langle\mathbf{F}\rangle_t = \int_S \langle\overleftrightarrow{\mathbf{T}}\rangle_t \cdot \hat{\mathbf{n}}\, dS. \quad (4)$$

Here $\overleftrightarrow{\mathbf{T}}$ is the Maxwell stress tensor, $\mathbf{E}$ is the electric field, $\mathbf{H}$ is the magnetic field, ϵ_w and μ_w are the permittivity and permeability of the surrounding medium (water), respectively, $\overleftrightarrow{\mathbf{I}}$ is the identity tensor, $\mathbf{F}$ is the net electromagnetic force acting on the particle, S is the outer surface of the nanoparticle, and $\hat{\mathbf{n}}$ is the surface normal to S. Here $\langle\cdot\rangle_t$ represents the time-averaged value. The time-averaged quantities can be directly obtained from the finite-element solver. Note that fields $\mathbf{E}$ and $\mathbf{H}$ in Eqs. (3) and (4) depend on the position of the particle. So for calculating force at a given point, the fields must be solved with the particle placed on that point. To map out the entire force field, the particle position is swept in a discrete 3D grid, and the fields and force values are recalculated for each case. The force value at an arbitrary point can be calculated from the discrete data set using interpolation. The force profiles obtained from this approach are shown in Figs. 5 and 6. For

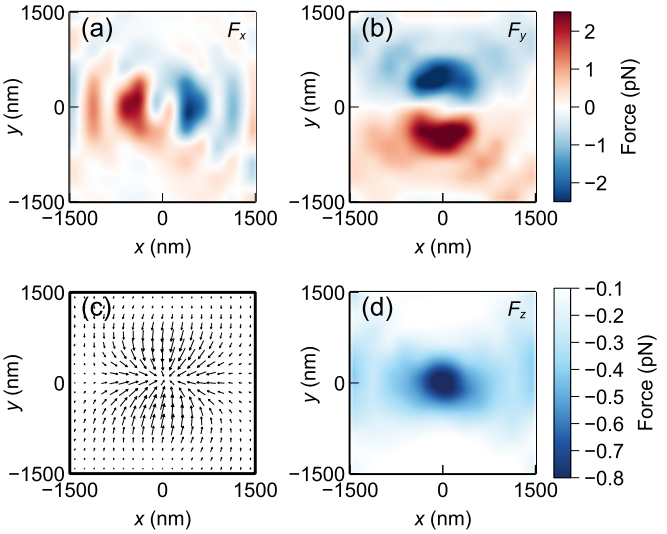

FIG. 5. Force profile for LHCP excitation at the $z = 660$ nm plane. (a) x component of the force F_x, (b) y component of the force F_y, (c) force lines in the xy plane, and (d) z component of the force F_z. Equations (3) and (4) were used to calculate the force.

visualization, $z = 660$ nm was selected as the representative surface because the force values in this plane are such that color map can show sufficient details for a wide region without saturating out the color in the strong-force areas. The force profile along the yz plane is shown in Fig. 7. It can be seen that the force magnitude decreases as the distance from the plasmonic surface increases. This is due to the exponentially decaying nature of the evanescent fields generated by the plasmonic structure [41].

For LHCP excitation, the force profile bears the characteristics of a conventional near-field trap. The particle is pulled towards the center of the structure. The force lines highlight

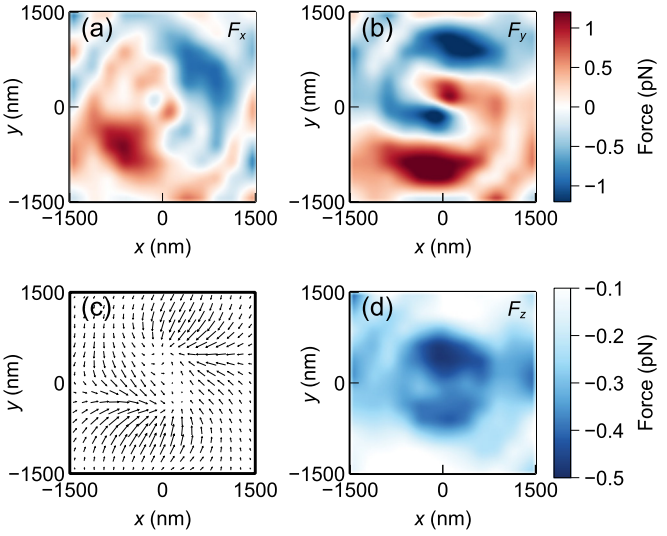

FIG. 6. Force profile for RHCP excitation at the $z = 660$ nm plane. (a) x component of the force F_x, (b) y component of the force F_y, (c) force lines in the xy plane, and (d) z component of the force F_z. Equations (3) and (4) were used to calculate the force.

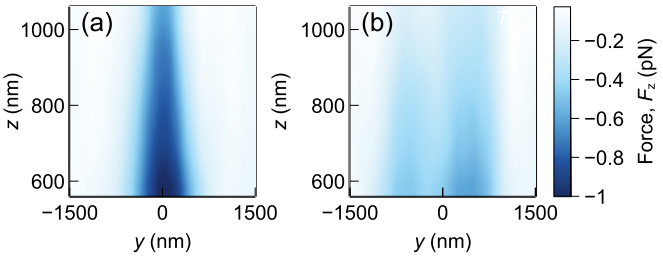

FIG. 7. z component of the force at the $x = 0$ plane for (a) LHCP excitation and (b) RHCP excitation. The plots share the same color bar. Equations (3) and (4) were used to calculate the force.

the gradient nature of the force. The force profile is much more complex for the RHCP excitation. Unlike the previous case, it is not intuitively obvious how a micro- or nanoparticle may move in such a force field. The usual approach of predicting a particle motion in a complex field involves simulating a large number of Brownian trajectories and conducting a statistical analysis. However, a deeper analysis of the force field may yield additional insight into the particle dynamics.

IV. THE HELMHOLTZ-HODGE DECOMPOSITION

In order to obtain a more intuitive understanding of the optical-force profiles, we decompose the vector field using the HHD method. According to the fundamental theorem of vector calculus, any sufficiently smooth vector field can be decomposed into a conservative (irrotational or curl-free) component $\mathbf{F}_{\text{cons}}$ and a solenoidal (divergence-free) component $\mathbf{F}_{\text{sol}}$:

$$\mathbf{F} = \mathbf{F}_{\text{cons}} + \mathbf{F}_{\text{sol}} = -\nabla u + \nabla \times \mathbf{A}\,. \tag{5}$$

Here u is a scalar potential function related to the conservative component, and $\mathbf{A}$ is a vector potential function related to the solenoidal component. For an optical force field $\mathbf{F}$ defined in a bounded domain Ω with a smooth boundary $\partial\Omega$, the HHD method can be applied to separate the components. The process involves solving the following partial differential equation (PDE) [42]:

$$\nabla^2 u = -\nabla \cdot \mathbf{F} \quad \text{on } \Omega\,, \tag{6}$$

with the boundary conditions

$$\nabla u \cdot \hat{\mathbf{n}} = \mathbf{F} \cdot \hat{\mathbf{n}} \quad \text{on } \partial\Omega\,. \tag{7}$$

Using the calculated optical force field $\mathbf{F}$, the PDE can be solved numerically to obtain u. Then, the two components can be easily calculated from $\mathbf{F}_{\text{cons}} = -\nabla u$ and $\mathbf{F}_{\text{sol}} = \nabla \times \mathbf{A} = \mathbf{F} - \mathbf{F}_{\text{cons}}$.

To determine which of these components is dominant, it is necessary to define parameters that quantify their relative magnitude. One such parameter could be the average ratio of their norms squared:

$$\bar{r}_{\text{norm}} = \left(\frac{\|\mathbf{F}_{\text{cons}}\|^2}{\|\mathbf{F}_{\text{sol}}\|^2} \right)_{\text{avg.}}. \tag{8}$$

TABLE II. Relative magnitude of the conservative component of the force.

Excitation polarization	Ratio of the norm squared $\bar{r}_{\text{norm}}$	Ratio of the squared volume integral $\langle r_{\text{vol}} \rangle_\Omega$
LHCP	257.03	67.80
RHCP	98.02	8.89

The following volume integral ratio could also be used for the same purpose:

$$\langle r_{\text{vol}} \rangle_\Omega = \frac{\int_\Omega \|\mathbf{F}_{\text{cons}}\|^2 \, d\Omega}{\int_\Omega \|\mathbf{F}_{\text{sol}}\|^2 \, d\Omega}. \tag{9}$$

Low values of $\bar{r}_{\text{norm}}$ and $\langle r_{\text{vol}} \rangle_\Omega$ indicate the presence of a strong solenoidal component. It should be noted that there is always the possibility of misinference when two vector fields are compared using a scalar number (such as the ratio of norms). To minimize the probability of such an occurrence, we use two parameters ($\bar{r}_{\text{norm}}$ and $\langle r_{\text{vol}} \rangle_\Omega$) that represent the same property but are calculated differently.

The decomposed components of the force field near a PAS for LHCP and RHCP excitations are shown in Figs. 8 and 9, respectively. The relative magnitudes of the components are listed in Table II. For LCHP excitation, $\mathbf{F}_{\text{cons}}$ makes up almost the entirety of the force field. This is expected as the force profile is similar to that of a gradient-trapping field. Particles in this force field are expected to be trapped near the center of the structure. More interesting results can be observed for the RHCP excitation case. For this case, the solenoidal component is much more prominent. Despite $\mathbf{F}_{\text{cons}}$ being larger (indicated by the fact that $\bar{r}_{\text{norm}} > 1$ and $\langle r_{\text{vol}} \rangle_\Omega > 1$), the effect of $\mathbf{F}_{\text{sol}}$ cannot be ignored. The force lines of $\mathbf{F}_{\text{cons}}$ show a few sink points. Looking at the lines more carefully, it can be inferred that $\mathbf{F}_{\text{cons}}$ may trap a particle in an annular region near the center of the structure. On the other hand, $\mathbf{F}_{\text{sol}}$ shows counterclockwise rotational force lines, suggesting that it would induce a rotational motion on a particle.

The force fields can be visualized more intuitively by using the vector-field-topology (VFT) method [31,32]. VFT is a representation of the global topology based on the analysis of critical points and their connections. By displaying only the critical points and the key integral lines (or streamlines) associated with those critical points, a vector field can be visualized more efficiently. By removing unimportant field lines, VFT produces a compressed intuitive representation of the field without losing relevant information. The codes used in this paper for the VFT visualization have been uploaded to GitHub [43]. For LHCP excitation, the VFT representation of the conservative component is shown in Fig. 8. Since the solenoidal component is negligible, a VFT visualization of that component is omitted. It can be noted that the conservative force component has two attracting nodes and one saddle point. Thus, the force acts like a near-field trap with two closely separated focal points. Figures 9(d) and 9(h) show the VFT representation of the conservative component and the solenoidal component, respectively, for the RHCP excitation

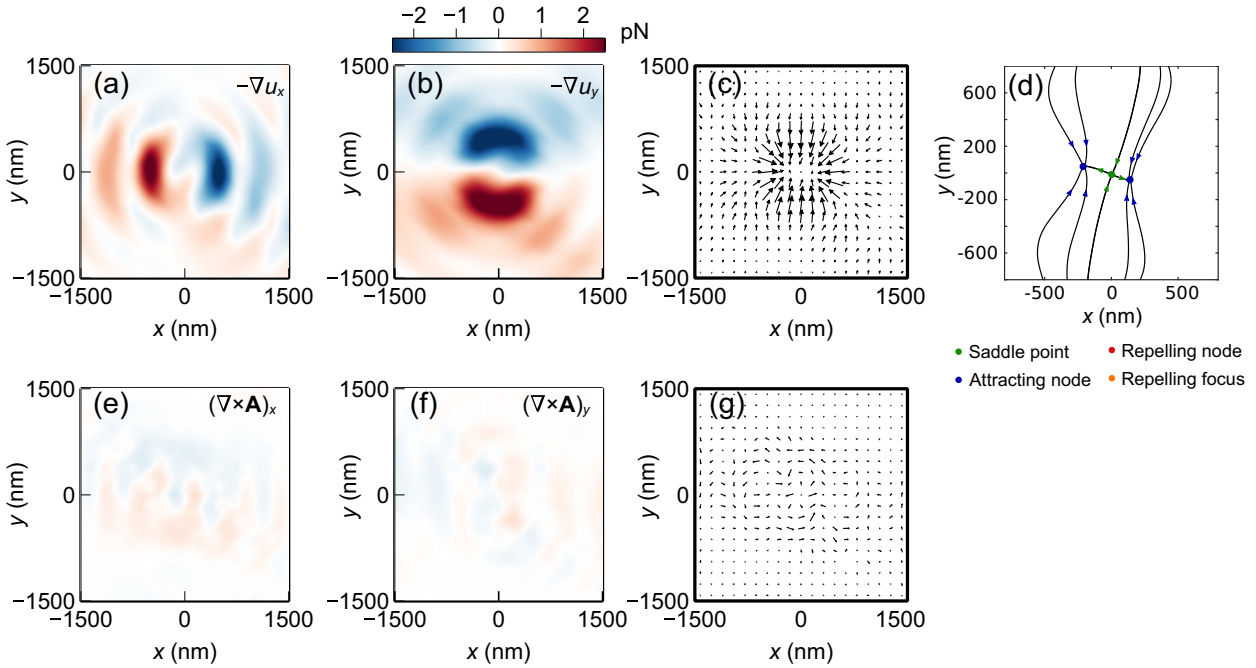

FIG. 8. Components of the optical force for LHCP excitation at the $z = 660$ nm plane. (a)–(d) The conservative component and (e)–(g) the solenoidal component. (a), (b), (e), and (f) share the same color bar. (d) is a visualization obtained using the vector-field topology method. The different colored points correspond to different types of critical points as described in the legend below (d). Equations (5), (6), and (7) were used on the LHCP force data to calculate force components.

case. The presence of two attracting nodes and two saddle points in an elliptical region along with a repelling node in the center can be observed in Fig. 9(d). This would imply that a particle would be repelled from the center and attracted towards the rim of an annular region. Figure 9(h) shows that the solenoidal component contains a repelling focus at the

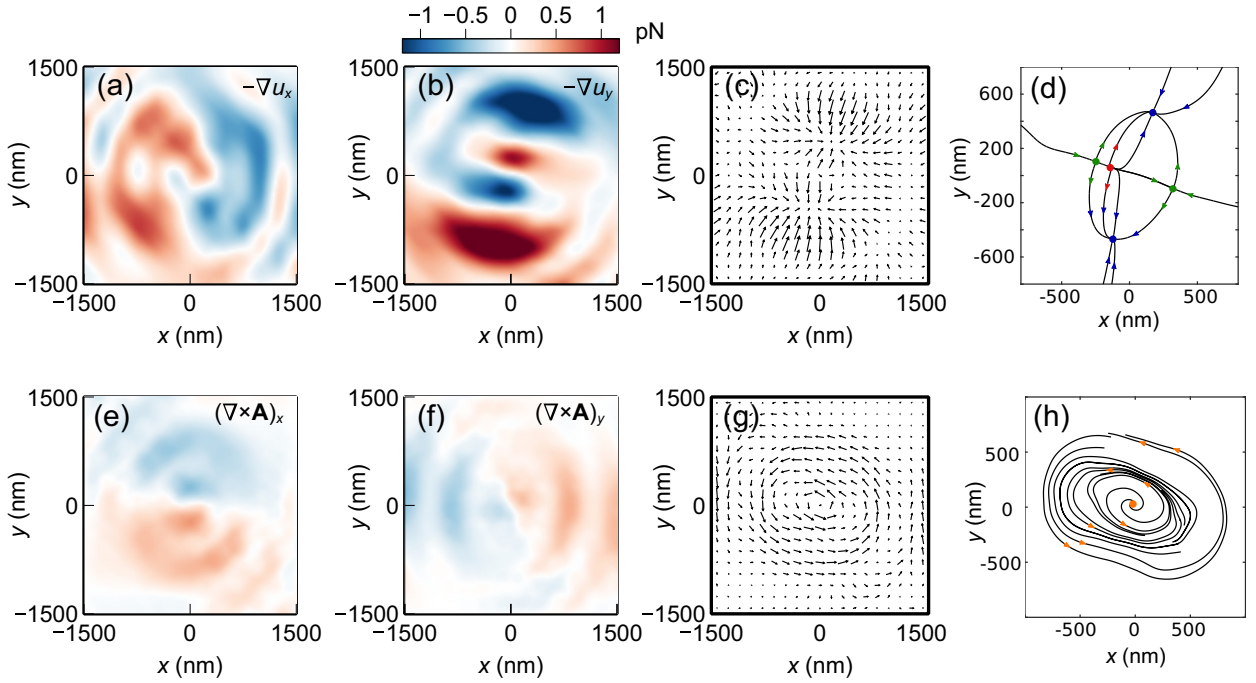

FIG. 9. Components of the optical force for RHCP excitation at the $z = 660$ nm plane. (a)–(d) The conservative component and (e)–(h) the solenoidal component. (a), (b), (e), and (f) share the same color bar. (d) and (h) are visualizations obtained using the vector-field topology method. The different types of critical points are represented using the color scheme mentioned in Fig. 8(d). Equations (5), (6), and (7) were used on the RHCP force data to calculate force components.

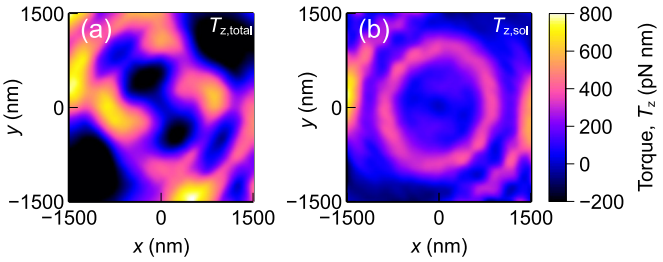

FIG. 10. The z component of the torque experience by the particle for RHCP excitation. (a) Torque calculated from the total force field and (b) torque calculated from the solenoidal component of the force. The axis of rotation is assumed to be the z axis. The plots share the same color bar.

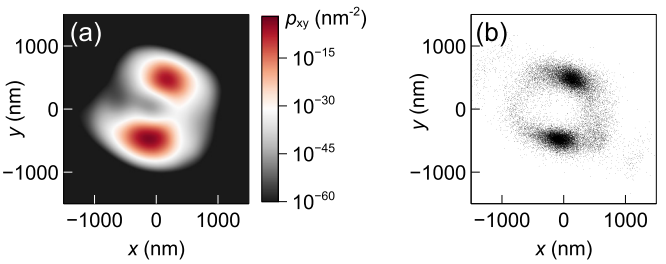

FIG. 12. For a PAS excited by 1545-nm RHCP light, (a) the position probability density of a particle calculated from optical potential and (b) the final position of 25,000 Brownian trajectories.

origin which creates a counterclockwise rotational motion. Thus, combining the effect of both components suggests that a particle immersed in this force field would rotate counterclockwise along an annular ring. This is consistent with the experimental results reported in [22].

The rotational motion can also be visualized by plotting the torque the particle experiences due to the generated force field. The torque can be easily calculated from the force field by using the point-particle approximation. Figure 10 shows the calculated torque. As the rotational motion occurs in the xy plane, we focus on only the z component of the torque. The z axis is assumed to be the axis of rotation for this calculation. It can be seen that the z component of the torque calculated from the solenoidal force has positive values around a circularly shaped region. This indicates a counterclockwise rotation along this path. Note that such a clear conclusion cannot be reached by observing the torque calculated from the total force. Hence, the advantage of using the HHD for intuitive understanding of optical forces is observed.

V. PARTICLE-POSITION DISTRIBUTION

The HHD gave us an intuitive understanding of how micro- or nanoparticles may behave in the optical force field near a PAS. The predictions made by the HHD analysis can be verified by calculating the position probability density function (pdf) of a micro- or nanoparticle in the force field. The position pdf can be approximated from Brownian dynamics simulation of a large number of independent trajectories [14,27]. It can also be approximated from the optical trapping potential [30,36]. The calculated position distributions are shown in Figs. 11 and 12. It can be noted that for LHCP excitation, the particle position distribution is concentrated in two closely separated points near (0,0) in the xy plane. The position of the high-probability region is consistent with the position of the attracting nodes shown in the VFT representations in Fig. 8(d). For RHCP excitation, the particle-position distribution is concentrated in an annular region. This is in agreement with the predictions of the HHD analysis. It should also be noted that the experimental results reported in [22] are also consistent with these results.

It can be noted from Fig. 12 that for the RHCP excitation case, the particle-position distribution does not follow a perfectly annular shape. One would expect a rotating particle motion would result in a uniform circular shape. The existence of two high-probability regions in the position density suggests that a particle is likely to spend more time on those regions compared to the others. So during the rotational motion of the particle, it would occasionally linger in these regions briefly. These high-probability regions coincide with the locations of the attracting nodes shown in Fig. 9(d). Thus, these two points act like localized traps and slow down the rotational motion of the particle. This behavior is also consistent with the experimental video provided in [22].

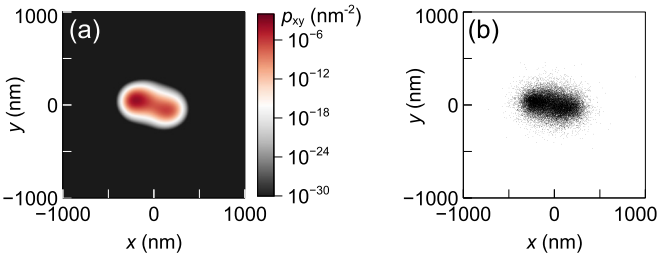

FIG. 11. For a PAS excited by 1545-nm LHCP light, (a) the position probability density of a particle calculated from the optical potential and (b) the final position of 25,000 Brownian trajectories.

VI. CONCLUSIONS

The force field near a PAS has been mapped and decomposed into conservative and solenoidal components. It has been found that for RHCP excitation, the structure produces a significant amount of solenoidal force, which induces rotational motion in trapped particles. This assessment is consistent with Brownian dynamics simulation and experimental results. The proposed decomposition technique can be used to gain intuitive understanding of the force near an optical trap. This can be beneficial in the design process of LOC systems.

ACKNOWLEDGMENTS

This work is supported by the National Institute of Health Grant No. 5R21HG009758. The authors thank Dr. Y.-T. Cheng, Dr. P. Hansen, and Dr. M. Yuen for their help.

[1] A. Ashkin, Phys. Rev. Lett. **24**, 156 (1970).
[2] A. Ashkin and J. Dziedzic, Appl. Phys. Lett. **19**, 283 (1971).
[3] A. Ashkin, Phys. Rev. Lett. **40**, 729 (1978).
[4] A. Ashkin and J. Dziedzic, Science **235**, 1517 (1987).
[5] M. D. Wang, H. Yin, R. Landick, J. Gelles, and S. M. Block, Biophys. J. **72**, 1335 (1997).
[6] M. Righini, P. Ghenuche, S. Cherukulappurath, V. Myroshnychenko, F. J. Garcia de Abajo, and R. Quidant, Nano Lett. **9**, 3387 (2009).
[7] T. Kuga, Y. Torii, N. Shiokawa, T. Hirano, Y. Shimizu, and H. Sasada, Phys. Rev. Lett. **78**, 4713 (1997).
[8] W. Ni, H. Ba, A. A. Lutich, F. Jackel, and J. Feldmann, Nano Lett. **12**, 4647 (2012).
[9] M. L. Juan, M. Righini, and R. Quidant, Nat. Photonics **5**, 349 (2011).
[10] K. Wang, E. Schonbrun, P. Steinvurzel, and K. B. Crozier, Nat. Commun. **2**, 469 (2011).
[11] K. Wang and K. B. Crozier, Chem. Phys. Chem. **13**, 2639 (2012).
[12] J. C. Ndukaife, A. V. Kildishev, A. G. A. Nnanna, V. M. Shalaev, S. T. Wereley, and A. Boltasseva, Nat. Nanotechnol. **11**, 53 (2015).
[13] Y. Zheng, J. Ryan, P. Hansen, Y.-T. Cheng, T.-J. Lu, and L. Hesselink, Nano Lett. **14**, 2971 (2014).
[14] P. Hansen, Y. Zheng, J. Ryan, and L. Hesselink, Nano Lett. **14**, 2965 (2014).
[15] M. Righini, A. S. Zelenina, C. Girard, and R. Quidant, Nat. Phys. **3**, 477 (2007).
[16] B. J. Roxworthy, K. D. Ko, A. Kumar, K. H. Fung, E. K. Chow, G. L. Liu, N. X. Fang, and K. C. Toussaint, Jr., Nano Lett. **12**, 796 (2012).
[17] P. Padhy, M. A. Zaman, and L. Hesselink, Opt. Lett. **44**, 2061 (2019).
[18] F. Afshinmanesh, J. S. White, W. Cai, and M. L. Brongersma, Nanophotonics **1**, 125 (2012).
[19] S. Yang, W. Chen, R. L. Nelson, and Q. Zhan, Opt. Lett. **34**, 3047 (2009).
[20] G. Rui, D. C. Abeysinghe, R. L. Nelson, and Q. Zhan, Sci. Rep. **3**, 2237 (2013).
[21] G. Rui, Q. Zhan, and Y. Cui, Sci. Rep. **5**, 13732 (2015).
[22] W.-Y. Tsai, J.-S. Huang, and C.-B. Huang, Nano Lett. **14**, 547 (2014).
[23] Y. Gorodetski, A. Drezet, C. Genet, and T. W. Ebbesen, Phys. Rev. Lett. **110**, 203906 (2013).
[24] J. I. Ziegler and R. F. Haglund, Nano Lett. **10**, 3013 (2010).
[25] J. I. Ziegler and R. F. Haglund, Plasmonics **8**, 571 (2013).
[26] C.-F. Chen, C.-T. Ku, Y.-H. Tai, P.-K. Wei, H.-N. Lin, and C.-B. Huang, Nano Lett. **15**, 2746 (2015).
[27] M. A. Zaman, P. Padhy, and L. Hesselink, Phys. Rev. A **96**, 043825 (2017).
[28] P. Padhy, M. A. Zaman, P. Hansen, and L. Hesselink, Opt. Express **25**, 26198 (2017).
[29] D. Fujiwara and H. Morimoto, J. Fac. Sci., Univ. Tokyo, Sect. 1A **24**, 685 (1977).
[30] M. A. Zaman, P. Padhy, P. C. Hansen, and L. Hesselink, Appl. Phys. Lett. **112**, 091103 (2018).
[31] J. Helman and L. Hesselink, Computer **22**, 27 (1989).
[32] J. L. Helman and L. Hesselink, IEEE Comput. Graphics Appl. **11**, 36 (1991).
[33] F. Maria Denaro, Int. J. Numer. Methods Fluids **43**, 43 (2003).
[34] M. Akram and V. Michel, GEM-Int. J. Geomath. **1**, 101 (2010).
[35] M. Bahl and P. Senthilkumaran, J. Opt. Soc. Am. A **29**, 2421 (2012).
[36] M. A. Zaman, P. Padhy, and L. Hesselink, Sci. Rep. **9**, 649 (2019).
[37] J. A. Hachtel, *The Nanoscale Optical Properties of Complex Nanostructures* (Springer, Cham, 2017).
[38] A. H. Yang, S. D. Moore, B. S. Schmidt, M. Klug, M. Lipson, and D. Erickson, Nature (London) **457**, 71 (2009).
[39] Q. Zhan, Opt. Lett. **31**, 867 (2006).
[40] C.-D. Ku, W.-L. Huang, J.-S. Huang, and C.-B. Huang, IEEE Photonics J. **5**, 4800409 (2013).
[41] M. A. Zaman, P. Padhy, and L. Hesselink, J. Appl. Phys. **122**, 163101 (2017).
[42] H. Bhatia, G. Norgard, V. Pascucci, and P.-T. Bremer, IEEE Trans. Visualization Comput. Graphics **19**, 1386 (2013).
[43] M. A. Zaman and L. Hesselink, Vector Field Topology 2D, https://github.com/zaman13/Vector-Field-Topolgy-2D.